Dichroism in two-color above-threshold ionization with twisted XUV beams and intense infrared laser fields

Baghdasar Baghdasaryan,[1,*] Birger Böning,[1,2] Willi Paufler,[1,2] and Stephan Fritzsche[1,2]
[1]*Theoretisch-Physikalisches Institut, Friedrich-Schiller-Universität Jena, D-07743 Jena, Germany*
[2]*Helmholtz-Institut Jena, D-07743 Jena, Germany*

(Received 28 November 2018; published 4 February 2019)

We theoretically investigate the two-color above-threshold ionization of atoms and ions by twisted XUV Bessel and Laguerre-Gaussian (LG) beams in the presence of a strong circularly polarized near-infrared (NIR) laser field. The presence of the NIR field modifies the continuum states accessible to the photoelectron. Based on the strong-field approximation, we explore the resulting energy and angular distributions of photoelectron as a function of the beam parameters. In particular, we analyze dichroism signals that arise due to the twisted nature of the XUV beam and the helicity of the NIR field. We focus on the comparison between LG beams and Bessel beams in the paraxial approximation. Here, we find that both beams yield similar results when the paraxial regime is valid. For localized targets, the dichroism signals strongly depend on the size and position of the atoms relative to the beam axis. Moreover, the dichroism signal tends to zero when the XUV LG beam is linear polarized. Detailed computations of the dichroism are performed and discussed for the 4*s* valence-shell photoionization of Ca^+ ions.

DOI: 10.1103/PhysRevA.99.023403

I. INTRODUCTION

The invention of the laser has made the detailed analysis of atomic and molecular ionization processes possible. In recent years, the ability to control laser fields of high intensity and short duration have lead to the discovery of various phenomena. A particular example is the above-threshold ionization (ATI) where a larger number of photons is absorbed than needed in order to overcome the ionization threshold [1]. Experimental and theoretical studies have investigated the influence of distinct laser parameters on ATI spectra, which has, in turn, lead to advances in laser technologies [2,3].

Moreover, the discovery of high harmonic generation (HHG) [4,5] and the invention of free-electron lasers (FELs) [6,7] enables one today the study of two-color multiphoton processes where one laser pulse is an extreme ultraviolet (XUV) field [8]. In such a process, a weak XUV pulse ionizes the atomic target. The photoelectron is subsequently released into a strong near-infrared (NIR) laser field. Such a two-color setup provides an experimental tool to analyze various aspects of light-matter interaction and dynamic processes within the atom. They have recently attracted much attention [7,9]. Especially, two-color multiphoton ionization of atomic helium was investigated using FEL-generated XUV radiation [6].

If the XUV pulse is long compared to the cycle length of the NIR field, the presence of the NIR field leads to the formation of sidebands around the main photoline [10,11]. These sidebands arise due to the emission or absorption of photons during the propagation of the photoelectron in the intense NIR field. Dichroism signals were used for the analysis of two-color ionization processes [12].

Apart from incident plane wave, the photoionization with so-called twisted light has been investigated in the past. In addition to spin angular momentum (SAM), twisted light also carries a nonvanishing orbital angular momentum (OAM). Experimental and theoretical studies have shown that the presence of this OAM strongly affects the photoionization of atoms [13,14]. Twisted light beams can now experimentally be generated using phase plates [15], axicons [16], or computer-generated holograms [17]. Moreover, XUV pulses carrying OAM can be generated also by using HHG and or even FEL facilities [18,19]. Experimentally, it was already demonstrated that the transfer of optical orbital angular momentum to the valence electron of a single trapped ion is possible with a vortex laser beam [20]. On the theoretical side, the twisted nature of the beam has been found to have a significant influence also on strong-field processes [21–23].

In this paper, we investigate the two-color ATI process where the usual plane-wave XUV field is replaced by a twisted light beam, which will be either a LG or a Bessel beam. For such a two-color process, we explore the dependence of the energy spectra and angular distribution of photoelectrons on the size and location of the atomic targets with regard to the common axis of the beams. Furthermore, we analyze effects that occur if the paraxial approximation is violated and show that the LG and Bessel beams yield quite similar results when the paraxial approximation is valid. Our analysis focuses on dichroism signals which occur due to a flip of the helicity of the NIR field or the OAM or helicity of the twisted beam. As was previously shown, this leads to a total of up to seven different dichroism signals [24]. On the experimental side, dichroism signals were used to measure the polarization state of a free-electron laser beam [25].

*baghdasar.baghdasaryan@uni-jena.de

This paper is structured as follows. In Sec. II A, we evaluate the transition amplitude for the two-color ATI of atoms with a weak XUV and a strong NIR field on the basis of the strong-field approximation (SFA). LG and Bessel beams as well as their characteristic parameters are introduced in detail in Sec. II B. The transition amplitude for the two-color ATI is then evaluated further in Sec. II D, and the dichroism signals are defined in Sec. II E. These dichroism signals and their dependence on the beam parameters are then discussed in detail in Sec. III. Finally, we conclude and give an outlook in Sec. IV.

Note that atomic units ($m_e = e = \hbar = 4\pi\varepsilon_0 = 1$) are used throughout the paper unless stated otherwise.

II. THEORETICAL METHODS

The setup of the two-color photoionization process is shown in Fig. 1. The twisted XUV beam (blue) and the NIR beam (orange) propagate in the z direction. The single atomic target is localized at impact parameter $\boldsymbol{b} = (b, \varphi_b = 0,\ z_b = 0)$ relative to the beam axis. Later, we will also consider targets that are extended over the cross section of the XUV beam. The emitted photoelectrons are measured at the detector with asymptotic momentum $\boldsymbol{p} = (p, \theta_p, \varphi_p)$. In the two-color ATI, moreover, we assume that the XUV beam is energetic enough to ionize the atomic target via single-photon absorption $\omega_X \gg E_B$, where E_B is the binding energy and ω_X is the XUV laser frequency. On the other hand, the NIR field is of rather high intensity so that it has to be considered in the dynamics of the photoelectron in the continuum. The NIR field is circularly polarized with helicity Λ_L. It is described by a vector potential $\boldsymbol{A}_L(t)$ that will be specified in Sec. II C. We assume that both fields are monochromatic and that the NIR field consists of many optical cycles.

A. Transition amplitude for two-color ATI

With the assumptions above, we can employ the SFA in order to investigate the two-color ATI. Within the SFA, it is assumed that the initial bound state of the atom is not affected by the NIR laser field. Moreover, the Coulomb potential of the parent ion is neglected in the final (continuum) state of the photoelectron. The continuum is then described by Volkov wave functions $\langle \Phi^{(V)}_{\boldsymbol{q}(t)}(t)| = \langle \boldsymbol{q}(t)|\, e^{-iS_V(t)}$, where $\boldsymbol{q}(t) = \boldsymbol{p} - \boldsymbol{A}_L(t)$ is the electron's kinetic momentum and the Volkov phase is given by [26]

$$S_V(t) = \frac{1}{2}\int_t^\infty dt' \frac{\boldsymbol{q}(t)^2}{2}.$$

The transition amplitude for the two-color ATI can then be written as [24]

$$\mathcal{T} = -i\int_{-\infty}^{\infty} dt\, \left\langle \Phi_p^{(V)}(t)\middle|\hat{\boldsymbol{p}}\cdot\boldsymbol{A}_X^C(\boldsymbol{r})\middle|\phi_o(t)\right\rangle e^{i(E_B-\omega_X)t}, \quad (1)$$

where $\langle\phi_0|$ is the initial bound state of the electron and $\boldsymbol{A}_X^C(\boldsymbol{r})$ is the vector potential of the XUV beam. Here the superscript C indicates that this vector potential is given in the Coulomb gauge, whereas the length gauge is applied for the NIR laser field in order to ensure that $\boldsymbol{p}$ is the conserved canonical momentum [27].

Below, we will analyze the transition amplitude (1) if the vector potential $\boldsymbol{A}_X^C(\boldsymbol{r})$ describes an LG or Bessel beam and discuss how the amplitude can be simplified for different beam parameters, such as the polarization, OAM, and the impact parameter of the atomic target. Before doing so, we will introduce LG and Bessel beams in detail in the next section.

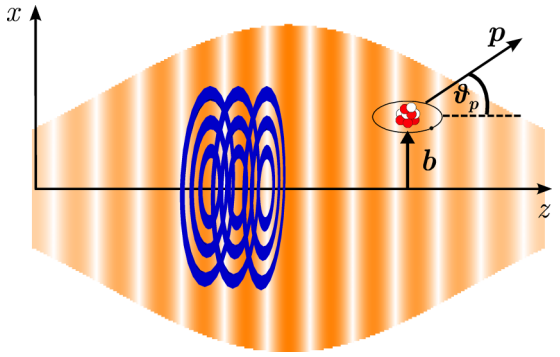

FIG. 1. Setup for the two-color ATI of an atom by a short twisted XUV beam (blue) and in the presence of a strong NIR field (orange). The vector $\boldsymbol{b}$ denotes the impact parameter of the target with regard to the common beam axis. The photoelectron is emitted with asymptotic momentum $\boldsymbol{p}$ under the polar emission angle θ_p.

B. Characterization of twisted light beams

Twisted light beams are characterized by helical wavefronts that lead to vanishing intensity on the beam axis. In cylindrical coordinates, the electric field of a twisted beam close to the beam axis has the form $E \propto r^{|m|}e^{im\varphi}$. Here, m is the so-called topological charge, which is defined as the number of twists around the axis that the phase experiences in one wavelength of propagation. A twisted beam of topological charge m carries an orbital angular momentum of $m\hbar$.

1. Bessel beams

The vector potential of any monochromatic light satisfies the Helmholtz equation [28],

$$(\Delta + k^2)\boldsymbol{A}(r) = 0, \quad (2)$$

where $k = \omega/c$ is the wave number of the electromagnetic field. Bessel beams represent a nonparaxial solution of the Helmholtz equation (2), which is also an eigenfunction of the projection of total angular momentum,

$$\hat{J}_z\boldsymbol{A}_X(\boldsymbol{r}) = m_\gamma \boldsymbol{A}_X(\boldsymbol{r}).$$

Following Ref. [29], the Bessel vector potential can be written as

$$\boldsymbol{A}_X^C(r) = \int \frac{d^2\boldsymbol{k}_\perp}{(2\pi)^2} a_{\varkappa m}(k_\perp) e^{i\boldsymbol{k}\cdot\boldsymbol{r}}\boldsymbol{\varepsilon}_c^C, \quad (3)$$

where the Fourier coefficients are given by

$$a_{\varkappa m}(k_\perp) = \sqrt{\frac{2\pi}{\varkappa}}(-i)^m e^{im\varphi_k}\delta(k_\perp - \varkappa).$$

These Fourier coefficients depend not only on the modulus of the transverse momentum $\varkappa = |\boldsymbol{k}_\perp|$, but also on the projection

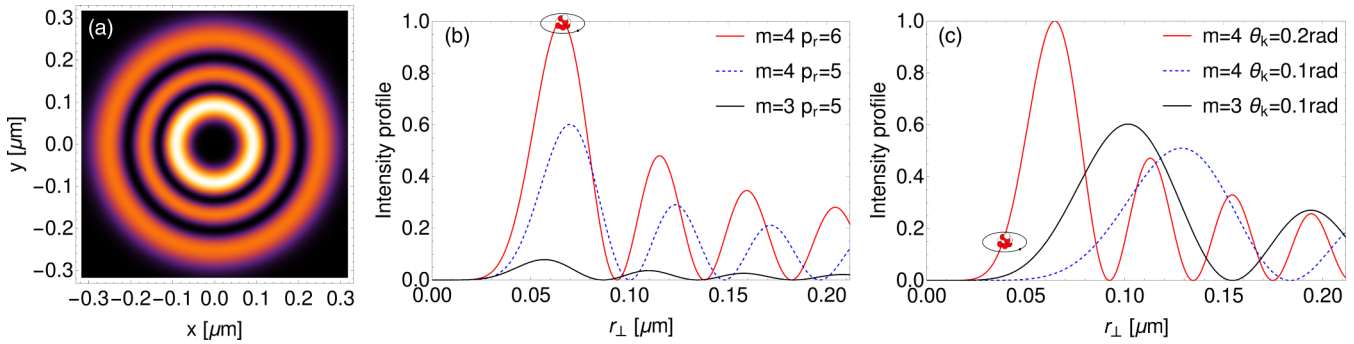

FIG. 2. Intensity profiles of LG and Bessel beams: (a) the intensity profile of the LG beam on the x-y plane at $z = 0$ for the radial index $p_r = 2$ and the OAM $m = 4$. (b) and (c) show the comparison of the transverse intensity profile for the LG and Bessel beams with different radial indices, opening angles, and OAM.

m of the OAM onto the beam axis. The polarization vector $\boldsymbol{\varepsilon}_c^C$ describes a circularly polarized plane wave with helicity $\Lambda_X = \pm 1$ and depends on orientation of $\boldsymbol{k}$ in momentum space,

$$\boldsymbol{\varepsilon}_c^C = \frac{-\Lambda_X}{\sqrt{2}} \begin{pmatrix} \cos\theta_k \cos\varphi_k - i\Lambda_X \sin\varphi_k \\ \cos\theta_k \sin\varphi_k + i\Lambda_X \cos\varphi_k \\ -\sin\theta_k \end{pmatrix}, \tag{4}$$

where θ_k is the so-called opening angle in momentum space. We note that, in the paraxial limit of small θ_k, we can write

$$\hat{J}_z \boldsymbol{A}_X(\boldsymbol{r}) = (m + \Lambda_X)\boldsymbol{A}_X(\boldsymbol{r}).$$

In order to make the intensity distribution in such a Bessel beam clearer, we consider its intensity profile given by the time-averaged Poynting vector. The z component of the Poynting vector of the Bessel beam (3) is given by [29]

$$P_z^B(r) = g_p \Lambda_X \frac{\varkappa k}{2\pi}\left[c_{+1}^2 J_{m+\Lambda_X-1}(\varkappa r_\perp) - c_{-1}^2 J_{m+\Lambda_X+1}(\varkappa r_\perp)\right],$$

where g_p is a proportionality constant and the expansion coefficients are given by

$$c_{\pm 1} = \tfrac{1}{2}(1 \pm \Lambda_X \cos\theta_k).$$

The transverse intensity profile is now given by $I_\perp(\boldsymbol{r}) = |P_z^B(\boldsymbol{r})|$. Its dependence on the OAM m and the opening angle θ_k is shown in Fig. 2 where the typical ringlike structure can be observed.

As a final remark, we note that monochromatic Bessel beams do not diffract, that is, the values of the transversal $\varkappa$ and longitudinal k_z components of the linear momentum are fixed. As a consequence, all wave-vectors $\boldsymbol{k}$ of the Bessel beam lie on a cone with an opening angle of θ_k [29]. Moreover, for monochromatic beams, only two of these four parameters k, θ_k, $\varkappa$, and k_z are independent, and the following relations apply:

$$\theta_k = \arctan(\varkappa/k_z), \quad \varkappa = \sqrt{k^2 - k_z^2}.$$

Therefore, a Bessel beam is fully defined by the four quantum numbers k, θ_k, Λ_X, and m.

2. LG beams

Another complete set of twisted beams are LG beams. Unlike Bessel beams, however, they do not represent exact solutions of the Helmholtz equation (2) but solve this in the paraxial limit. This limit follows from the Helmholtz equation (2) if we assume that the ray inclination to the optical axis is small. As before, we consider a beam propagating in the z direction,

$$\boldsymbol{A}^L(r) = \boldsymbol{\varepsilon}^L u(\boldsymbol{r}) \exp(ikz), \tag{5}$$

where $u(\boldsymbol{r})$ is an amplitude distribution and $\boldsymbol{\varepsilon}^L$ is the polarization vector. In contrast to Bessel beams, we here use the Lorentz gauge, indicated by the superscript L since the Coulomb gauge requires the vanishing of the divergence of the vector potential, which leads to complications in the paraxial approximation. The beam is supposed to be transverse, i.e., the polarization vector $\boldsymbol{\varepsilon}^L$ lies on the x-y plane [30]. Note that, since the polarization vector appears as a factor in Eq. (5), LG beams can be circularly, linearly, or elliptically polarized. This is in contrast to Bessel beams, that are always characterized by a well-defined helicity Λ.

Substitution of the vector potential (5) into the Helmholtz equation (2) yields

$$\nabla_\perp^2 u + 2ik\frac{\partial u}{\partial z} + \frac{\partial^2 u}{\partial^2 z} = 0. \tag{6}$$

If we assume a well-collimated beam, the profile $u(\boldsymbol{r})$ changes slowly with z compared to the phase factor $\exp(ikz)$. Furthermore, if this z dependence is slow compared to the transverse variation of the profile $u(\boldsymbol{r})$, the paraxial approximation is valid [31]

$$\left|\frac{\partial^2 u}{\partial z^2}\right| \ll \left|2k\frac{\partial u}{\partial z}\right|, \quad \left|\frac{\partial^2 u}{\partial z^2}\right| \ll |\nabla_\perp^2 u|.$$

The wave Eq. (6) can then be approximately written as

$$\nabla_\perp^2 u + 2ik\frac{\partial u}{\partial z} = 0. \tag{7}$$

The solution of the paraxial wave equation (7) representing LG beams is given in cylindrical coordinates by [32]

$$u(r_\perp, \varphi, z) = \frac{1}{\omega(z)}\left(\frac{\sqrt{2}r_\perp}{\omega(z)}\right)^{|m|} \exp\left[-\frac{r_\perp^2}{\omega^2(z)}\right] L_{p_r}^{|m|}\left[\frac{2r_\perp^2}{\omega^2(z)}\right] \times \exp\left[im\varphi + \frac{ikr_\perp^2 z}{2(z^2 + z_R^2)} - i(2p_r + m + 1) \times \arctan\left(\frac{z}{z_R}\right)\right].$$

Here, $L_p^{|m|}$'s are the associated Laguerre polynomials, and $\omega(z) = \omega_0\sqrt{1+z^2/z_R^2}$ is the radius of the beam with the beam-waist ω_0 and the Rayleigh range $z_R = k\omega_0^2/2$. The radial quantum index p_r defines the number of rings in the intensity profile of the LG beam. Moreover, LG modes satisfy an orthogonality relation with respect to the beam waist, i.e., the scalar product between two LG modes with beam-waist parameters ω_0 and ω_0' vanishes unless $\omega_0 = \omega_0'$ [33].

To end this section, let us consider the intensity profile of the LG beams. The z component of the Poynting vector for both linearly and circularly polarized LG beams is given by [32]

$$P_z^{\mathrm{LG}}(r_\perp,\varphi) = \frac{1}{\omega(z)^2}\left(\frac{\sqrt{2}r_\perp}{\omega(z)}\right)^{2|m|}\exp\left[-\frac{2r_\perp^2}{\omega^2(z)}\right] \times\left(L_{p_r}^{|m|}\left[\frac{2r_\perp^2}{\omega^2(z)}\right]\right)^2.$$

The intensity profiles are shown in Fig. 2. As can be seen, the intensity profile of a LG beam is also radially symmetric.

Finally, we note that the LG beams are completely defined by the five parameters p_r, m, λ, ε, and ω_0. Unlike in the case of Bessel beams, the opening angle of the LG beam,

$$\theta_k(\varkappa) = \arctan\left[\frac{\varkappa}{\sqrt{\omega_x^2/c^2-\varkappa^2}}\right]$$

is not constant, which implies that the beam is diffracting.

C. Evaluation of the transition amplitude

We now turn to the evaluation of the transition amplitude (1) if the ionizing XUV beam either describes a Bessel or a LG beam. For a Bessel beam, this transition has been discussed in detail in Ref. [24]. Therefore, we will here restrict ourselves to the derivation in the latter case. In order to evaluate the transition amplitude (1) for a LG beam, we represent its vector potential (5) as a superposition of plane waves [34],

$$\boldsymbol{A}_X^L(\boldsymbol{r}) = \int d^2\boldsymbol{k}_\perp \boldsymbol{\varepsilon}^L \upsilon_{p_r m}(k_\perp) e^{i\boldsymbol{k}\cdot\boldsymbol{r}},$$

where the Fourier coefficients are given by

$$\upsilon_{pm}(k_\perp) = \frac{(-i)^m\omega_0}{4\pi}e^{-k_\perp^2\omega_0^2/4}e^{im\varphi_k}\left(\frac{k_\perp\omega_0}{2}\right)^{|m|} \times\sum_{\beta=0}^{p_r}(-1)^\beta 2^{\beta+|m|/2}\binom{p_r+|m|}{p_r-\beta}L_\beta^{|m|}\left(\frac{k_\perp^2\omega_0^2}{4}\right).$$

As mentioned before, the XUV vector potential in the transition amplitude (1) is given in the Coulomb gauge. We, therefore, perform a gauge transformation of the LG vector potential [31],

$$\boldsymbol{A}^C = \frac{\boldsymbol{\nabla}(\boldsymbol{\nabla}\boldsymbol{A}^L)}{k^2} + \boldsymbol{A}^L. \tag{8}$$

Below, we focus on either a linear polarization along the x direction or a circular polarization with helicity Λ_X. In both cases, the gauge transformation Eq. (8) yields

$$\boldsymbol{A}_X^C(r) = \int d^2\boldsymbol{k}_\perp \boldsymbol{\varepsilon}_{l,c}^C \upsilon_{pm}(k_\perp) e^{i\boldsymbol{k}\cdot\boldsymbol{r}}, \tag{9}$$

where the subscripts l and c denote linear and circular polarizations, respectively.

The polarization vector $\boldsymbol{\varepsilon}_l^C$ for the case of linear polarization is given by

$$\boldsymbol{\varepsilon}_l^C = \frac{1}{2}\begin{pmatrix}2-2\,\sin^2\theta_k\cos^2\varphi_k\\ -\sin^2\theta_k\sin(2\varphi_k)\\ -\sin(2\theta_k)\cos\,\varphi_k\end{pmatrix}.$$

The polarization vector $\boldsymbol{\varepsilon}_c^C$ for circular polarization is identical to the one given for Bessel beams in Eq. (4).

As long as the photoelectron propagates in the NIR laser field, the kinetic momentum $\boldsymbol{q}(t) = \boldsymbol{p} - \boldsymbol{A}_L(t)$ and the conserved canonical momentum $\boldsymbol{p}$ are different. The vector potential of the NIR field is given by

$$\mathbf{A}_L(t) = A_L[\cos(\omega_L t)\boldsymbol{e}_x + \Lambda_L\sin(\omega_L t)\boldsymbol{e}_y],$$

with the helicity Λ_L.

We can evaluate the scalar product of the kinetic momentum and polarization vector $\boldsymbol{q}(t)\cdot\boldsymbol{\varepsilon}_{l,c}^C$, which arises after substitution of the vector potential (9) into the transition amplitude (1). This scalar product characterizes the angular distribution of the emitted photoelectrons and the strength of the sideband amplitudes. For circular polarization, we find

$$\begin{aligned}\boldsymbol{q}(t)\cdot\boldsymbol{\varepsilon}_c^C = -\Lambda_X\frac{p}{\sqrt{2}}\Big[&\sin\theta_p e^{i\Lambda_X(\varphi_p-\varphi_k)} - 2\,\sin\theta_p\sin^2\frac{\theta_k}{2}\\ &\times\cos(\varphi_p-\varphi_k) - \cos\theta_p\sin\theta_k\Big]\\ &+\Lambda_X\frac{A_L}{\sqrt{2}}\Big[e^{i\Lambda_X(\Lambda_L\omega_L t-\varphi_k)} - \sin^2\frac{\theta_k}{2}(e^{i\omega_L t}e^{-i\Lambda_L\varphi_k}\\ &+e^{-i\omega_L t}e^{i\Lambda_L\varphi_k})\Big].\end{aligned} \tag{10}$$

We note that this scalar product and, hence, the sideband amplitudes depend on the particular direction of the wave-vector $\boldsymbol{k}$.

In the case of linear polarization, the scalar product can be written as

$$\begin{aligned}\boldsymbol{q}(t)\cdot\boldsymbol{\varepsilon}_l^C = &F(\theta_k,\varphi_k) + C(\theta_k,\varphi_k)e^{-i\omega_L\Lambda_L t}\\ &+C(\theta_k,-\varphi_k)e^{i\omega_L\Lambda_L t},\end{aligned} \tag{11}$$

where

$$\begin{aligned}F(\theta_k,\varphi_k) = p\{&\sin\theta_p\cos\varphi_p + \sin\theta_k\cos\varphi_k[\cos\theta_p\cos\theta_k\\ &+\cos(\varphi_k-\varphi_p)\sin\theta_p\sin\theta_k]\},\end{aligned}$$

and

$$C(\theta_k,\varphi_k) = \frac{A_L}{2}[\sin^2\theta_k\cos\varphi_k e^{i\varphi_k} - 1].$$

The first term in Eq. (11) arises from the interaction with the XUV field. This can be seen from $A_L \to 0$. The product becomes maximal when $\boldsymbol{q}(t)$ and the polarization vector are parallel.

The transition amplitude (1) can be analytically expressed if we consider a sufficiently weak NIR laser field, compared to the asymptotic momentum $p \gg A_L$. Furthermore, since the laser intensity is not high enough to cause relativistic effects and the wavelength of the laser field is larger than the size of an atomic system, we may employ the dipole approximation. Based on these assumptions, the transition amplitude (1) was already calculated for the case of an XUV Bessel beam in Ref. [24]. We find an analogous expression if the vortex XUV beam is an LG beam with vector potential (9),

$$\mathcal{T}_{\boldsymbol{b}}(\boldsymbol{p}) = 2\pi \sum_l \delta(p^2/2 + U_p + E_B - \omega_\chi - l\omega_L)\mathcal{T}^l,$$

where the *partial amplitudes*,

$$\mathcal{T}^l = \int d^2\boldsymbol{k}_\perp \upsilon_{pm}(\boldsymbol{k}_\perp) e^{i\boldsymbol{b}\boldsymbol{k}} B_l(k_\perp, \varphi_k, \Lambda_L) \tag{12}$$

describe the individual sidebands in the photoelectron spectrum. Similar to the case of an XUV Bessel beam, the Fourier coefficients of the XUV beam, υ_{pm}, and the modified sideband amplitudes $B_l(k_\perp, \varphi_k, \Lambda_L)$ appear in Eq. (12). We replace $\boldsymbol{r} \to \boldsymbol{b} + \boldsymbol{r}$ since $\boldsymbol{r}$ denotes the electronic coordinate with respect to the atomic nucleus, which is located at the impact parameter $\boldsymbol{b}$ and represents the center of the atomic potential. Therefore, the phase factor $e^{i\boldsymbol{b}\boldsymbol{k}}$ arises in Eq. (12). It can be seen that the sideband amplitudes depend only on the scalar products (10) and (11). For the special case of a linearly polarized LG beam, we find

$$B_l(k_\perp, \varphi_k, \Lambda_L) = N(l)F(\theta_k, \varphi_k) + N(l - \Lambda_L)C(\theta_k, \varphi_k) + N(l + \Lambda_L)C(\theta_k, -\varphi_k),$$

with

$$N(l) = -i2\pi J_l(\alpha_L) e^{il\Lambda_L\varphi_p} \langle p_l | \phi_o(t) \rangle. \tag{13}$$

We note that the modulus of the photoelectron momentum depends on sidebands number l and is given by $|\boldsymbol{p}| = p_l = \sqrt{2(\omega_X + l\omega_L - E_B - U_p)}$.

D. Photoionization probability for localized and macroscopically extended targets

We can apply the the partial amplitudes (12) to compute the photoionization probability for individual sidebands,

$$\mathrm{P}_{\boldsymbol{b}}^{(l)}(\boldsymbol{p}) = |\mathcal{T}^{(l)}|^2. \tag{14}$$

This expression describes the photoionization probability of a single atom located at some impact parameter $\boldsymbol{b}$ and for a particular sideband number l. If we consider the extended target that consists of an atomic cloud with density distribution $\rho(\boldsymbol{b})$, we have to sum the photoionization probabilities $P_{\boldsymbol{b}}^{(l)}(\boldsymbol{p})$ over all impact parameters $\boldsymbol{b}$,

$$P^{(l)}(\boldsymbol{p}) = \int d^2\boldsymbol{b}\, \rho(\boldsymbol{b}) P_{\boldsymbol{b}}^{(l)}(\boldsymbol{p}). \tag{15}$$

In the following, we consider the cases of an infinitely extended homogeneous target and a Gaussian distribution of atoms, respectively, given by

$$\rho(\boldsymbol{b}) = 1,$$

and

$$\rho(\boldsymbol{b}) = \frac{1}{\sqrt{2\pi}\sigma_b} \exp\left(-\frac{(\boldsymbol{b} - \boldsymbol{b}_0)^2}{2\sigma_b^2}\right).$$

The size of the target plays an important role in the interpretation of experimental results. Especially, the influence of the SAM and the OAM of the XUV beam on the photoionization becomes less pronounced as the target size σ_b increases. For an infinitely extended homogeneous target ($\rho = 1$), the partial ionization probabilities become

$$P^{(l)}(\boldsymbol{p}) = \int d^2\boldsymbol{k}_\perp d^2\boldsymbol{k}'_\perp d^2\boldsymbol{b}\, \upsilon_{pm}(k_\perp)\upsilon^*_{pm}(k'_\perp) e^{i\boldsymbol{b}(\boldsymbol{k}-\boldsymbol{k}')} \times B_l(k_\perp, \varphi_k, \Lambda_L) B_l^*(k'_\perp, \varphi'_k, \Lambda_L).$$

The integration over the impact parameter $\boldsymbol{b}$ yields a Dirac δ distribution in k space,

$$\int d^2\boldsymbol{b}\, e^{i\boldsymbol{b}(\boldsymbol{k}-\boldsymbol{k}')} = 2\pi\delta(\boldsymbol{k} - \boldsymbol{k}').$$

Therefore, the partial ionization probability for an infinitely extended homogeneous target can be simplified to give

$$P^{(l)}(\boldsymbol{p}) = 2\pi \int d^2\boldsymbol{k}_\perp |\upsilon_{pm}(k_\perp)|^2 |B_l(k_\perp, \varphi_k, \Lambda_L)|^2. \tag{16}$$

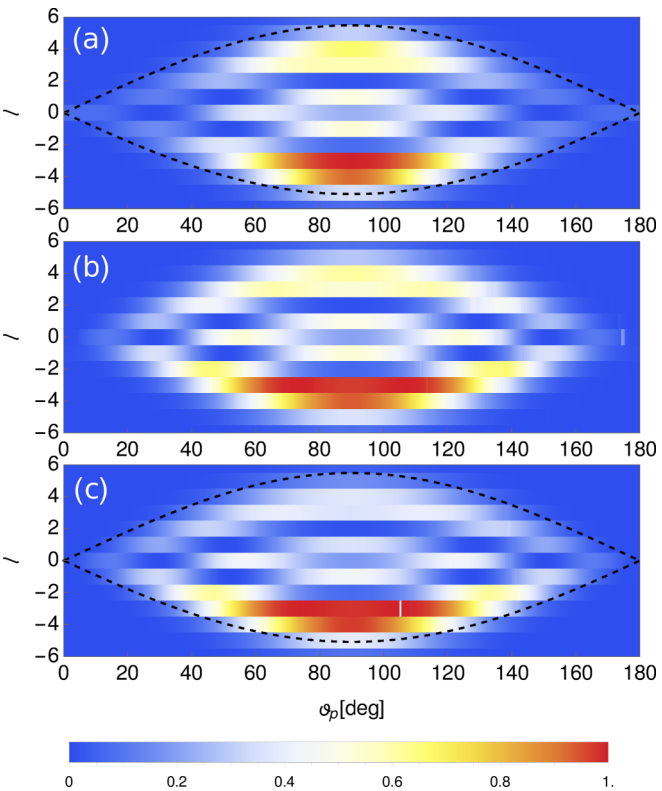

FIG. 3. Photoionization probabilities $P^{(l)}(\boldsymbol{p})$ for a macroscopic atomic target as a function of the sideband number l and the emission angle θ_p. The calculation was performed for (a) an XUV Bessel beam with opening angle $\theta_k = 0.2$ rad and frequency $\omega_X = 3$ a.u. = 81.6 eV, (b) a circularly polarized XUV LG beam, and (c) a linearly polarized XUV LG beam with frequency $\omega_X = 3$ a.u. and beam-waist $\omega_0 = 100$ nm. The chosen parameters for the NIR field are $A_L = 0.1$ a.u. and $\omega_X = 0.05$ a.u. = 1.36 eV.

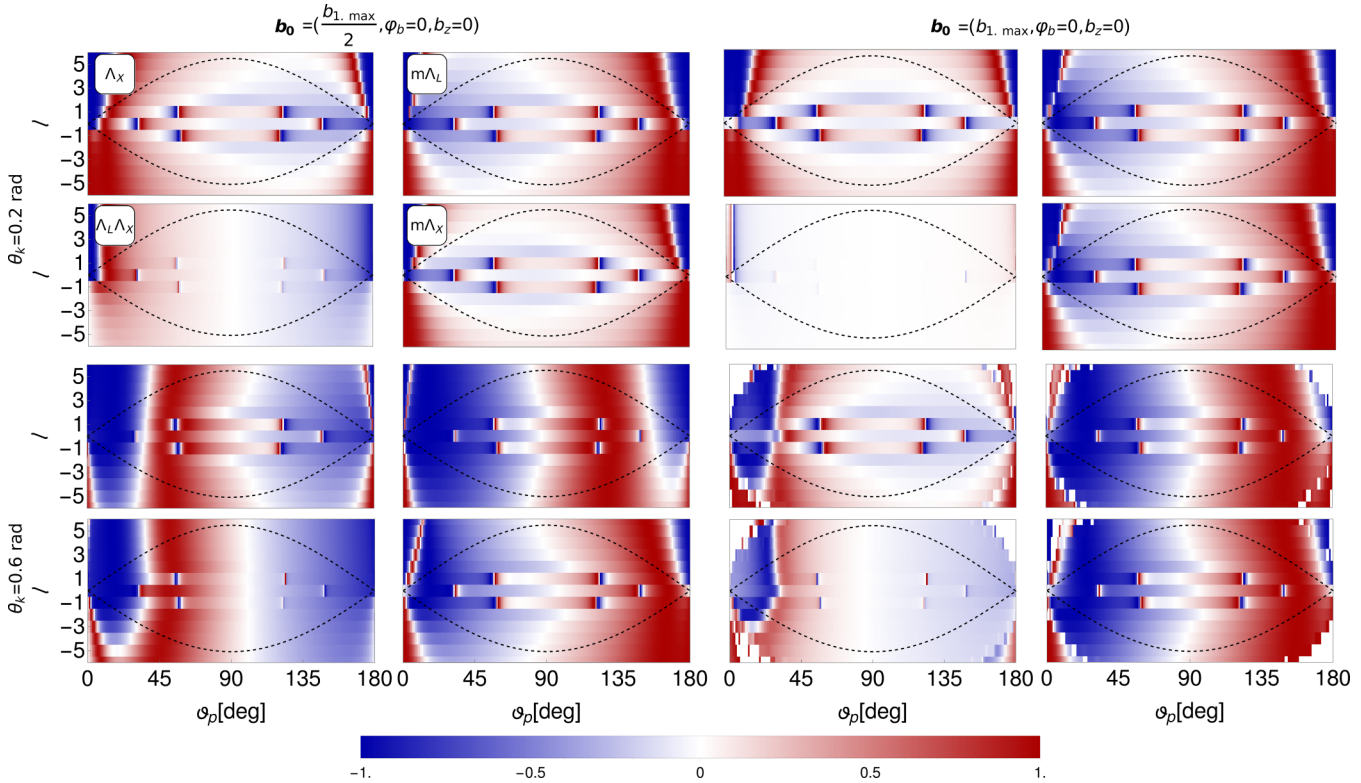

FIG. 4. Dichroism signals for the two-color photoionization of the 4s valence shell of Ca^+ as a function of the emission angle θ_p and the sideband number l. Results are shown for Bessel beams with opening angles $\theta_k = 0.2$ and $\theta_k = 0.6$ rad, respectively, photon energy $\omega_X = 3$ a.u. $= 81.6$ eV, and with the OAM $m = 4$. The atomic target is placed on two different impact parameters b_0, namely, on the first maximum of transverse intensity on the x-y plane and on the half of this impact parameter. The target size is $\sigma_b = 10$ nm. The photoelectrons are observed at the azimuthal angle $\varphi_p = \pi/2$. The black dotted curves indicate the sideband cutoffs.

In the following, the integrals in Eqs. (15) and (16) are evaluated numerically.

E. Dichroism in two-color fields

The photoionization probability (15) for a given sideband number l depends not only on the emission angles θ_p and φ_p, but also on the quantum numbers of the ionizing beam that were discussed in Sec. II B. In order to analyze the dependencies on the helicities Λ_L, Λ_X, and the OAM m, we now introduce dichroism signals.

From two-color experiments with plane XUV and NIR fields, the *circular* dichroism is well known [35] and defined as the ratio of the difference in photoionization probability for the right and left circularly polarized beams and the sum of these probabilities,

$$D^{(\mathrm{circ.})} = \frac{P^{(\mathrm{right})} - P^{(\mathrm{left})}}{P^{(\mathrm{right})} + P^{(\mathrm{left})}}. \tag{17}$$

If the incident beam is twisted and circularly polarized, we can define seven dichroism signals by changing the sign of quantum numbers Λ_L, Λ_X, and m and their combinations, analogous to Eq. (17). For instance, the dichroism associated with a flip of the projection of OAM m and helicity of the NIR laser field can be presented as

$$D^{(m\Lambda_L)} = \frac{P(\boldsymbol{p}, m, \Lambda_X, \Lambda_L) - P(\boldsymbol{p}, -m, \Lambda_X, -\Lambda_L)}{P(\boldsymbol{p}, m, \Lambda_X, \Lambda_L) + P(\boldsymbol{p}, -m, \Lambda_X, -\Lambda_L)}.$$

The definitions of such dichroism signals were discussed in detail in Ref. [24]. However, if the XUV field is linearly polarized, we can just define three dichroism signals associated with a flip of the signs of m, Λ_L, and $m\Lambda_L$.

III. RESULTS AND DISCUSSION

In the previous sections, we derived an expression for the two-color photoionization probabilities (14) and (15) for two types of twisted light combined with an intense NIR plane-wave laser field. Our emphasis in the discussion will be placed on the dependence of the dichroism signals on the characteristic quantum numbers defining the twisted beams. In more detail, we consider the ionization of the 4s valence electron of Ca^+ with a binding energy of $E_B = 0.49$ a.u $= 11.7$ eV. For the LG beam, we choose the following parameters: the beam-waist $\omega_0 = 100$ nm, the radial index $p_r = 6$, the projection of the OAM $m = 4$, and frequency $\omega_X = 3$ a.u. $= 81.6$ eV. For the Bessel beam, we choose the same OAM and frequency as for the LG beam and opening angles of $\theta_k = 0.2$ and $\theta_k = 0.6$ rad, respectively. For the NIR field, we choose an amplitude of $A_L = 0.1$ a.u. and the frequency $\omega_L = 0.05$ a.u. $= 1.36$ eV.

Figure 3 displays the photoionization probabilities of the two-color ATI as a function of the sideband number l and emission angle θ_p. The calculation was performed for an infinitely extended macroscopic target. The photoionization probabilities were evaluated for a Bessel beam (upper panel),

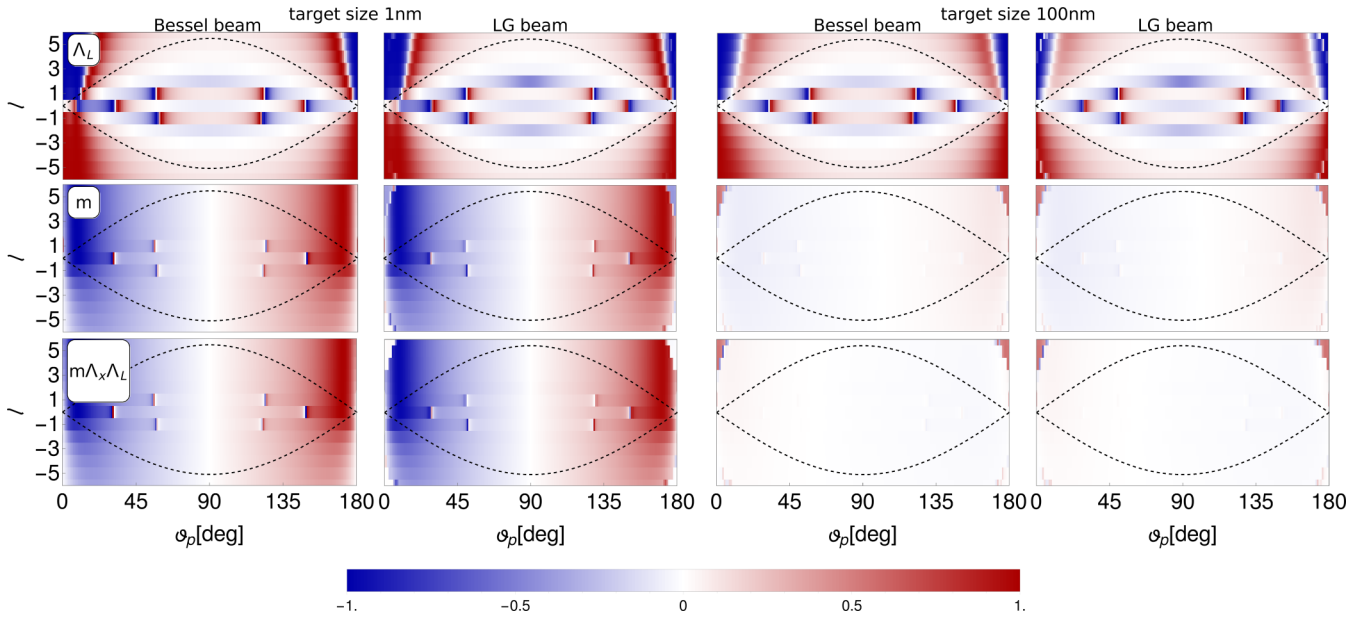

FIG. 5. The same as in Fig. 4 but for a Bessel beam with opening angle $\theta_k = 0.2$ rad and a LG beam with beam-waist $\omega_0 = 65$ nm, respectively. The photon energy of both beams is $\omega_X = 3$ a.u. $= 81.6$ eV and the OAM $m = 4$. The atomic target is placed at impact parameter $b_0 = 65$ nm. As target sizes are chosen, $\sigma_b = 1$ nm (first and second columns) and $\sigma_b = 100$ nm (third and fourth columns). The photoelectrons are observed at the azimuthal angle $\varphi_p = \pi/2$. The black dotted curves indicate the sideband cutoffs.

circularly polarized LG beam (middle panel), and linearly polarized LG beam (lower panel).

The black dotted curves indicate the cutoff values $\pm l_{\max}$ of the number of sidebands that were calculated using the properties of Bessel functions [36]. For $l > |l_{\max}|$, the photoionization probability decreases exponentially with l. In other words, a meaningful measurement of dichroism signals in this area is not possible. The maximal number of sidebands occurs at $\theta_p = \pi/2$ where the emission direction is on the polarization plane of the NIR laser field. The probability to emit a NIR photon ($l < 0$) is higher than to absorb it ($l > 0$) in all three cases. The reason for this behavior is the matrix element in Eq. (13), which also decreases with increasing p_l. In other words, the density of the initial state increases with decreasing momentum.

In order to analyze the dependence of the photoionization probability on the beam parameters of the XUV vortex beams, we consider the dichroism signals defined in Sec. II E. We here first consider a localized atomic cloud centered around impact parameter b_0. Let us start with the Bessel beam and discuss effects that occur when the impact parameter b_0 or the opening angle θ_k, respectively, are varied (see Fig. 4). Dichroism signals were evaluated for the opening angles $\theta_k = 0.2$ and $\theta_k = 0.6$ rad. The atomic target was placed at the first intensity maximum $b_0 = b_{1\,\max}$ and at half of this value $b_0 = b_{1\,\max}/2$, respectively (see Fig. 2). The dichroism associated with the product $\Lambda_X\Lambda_L$ decreases in the region of the intensity maximum and vanishes if the target is placed on the first intensity maximum for small opening angle θ_k, Fig. 4. Obviously, the dichroism signals associated with flips of Λ_L and Λ_X are identical in this case. The reason for this behavior is that the XUV Bessel beam for small atomic targets can be approximated in a region near to the first maximum as a plane wave. The dichroism is the same independent of which helicity is reversed (IR or XUV). The full width at half maximum of the first intensity maximum in Fig. 2 decreases when the opening angle θ_k is increased. Here, the deviation of the Bessel beam from the plane wave becomes noticeable. The dichroism signal that is associated with a flip of the sign of $\Lambda_X\Lambda_L$ increases with increasing θ_k. Another effect associated with the increase in opening angle θ_k is the coupling of the OAM and helicity Λ_L. The quantum number m of the Bessel beam is well defined only in the paraxial approximation. If the sign of Λ_X is changed while keeping the OAM, the beam remains unchanged in the paraxial approximation, except for the polarization direction. In general, however, the OAM m and the helicity Λ_X couples outside of the paraxial regime, and hence, a change in Λ_X affects the global beam characteristics. In other words, the flip of helicity Λ_X for large opening angles of the Bessel beam has more influence on the OAM m than in paraxial approximation and leads, therefore, to a stronger dichroism signal for large θ_k.

Figure 5 compares the dichroism signals for Bessel and LG beams. The first and second columns in this represent the dichroism for a small atomic target with $\sigma_b = 1$ nm for circularly polarized Bessel and Laguerre beams, respectively. Similarly, the third and fourth columns represent the same but for a target size of $\sigma_b = 100$ nm, which is larger in comparison to the width of an intensity maximum of the corresponding beams. The dichroism is presented as a function of the number of individual sidebands l and the emission angle θ_p. The target of atoms is located on impact parameter $b_0 = 65$ nm [indicated in Fig. 2(b)].

Similar as for a LG XUV beam, the orbital and spin angular momenta of Bessel beams decouple within the paraxial approximation. We, therefore, expect that these two beams

behave similarly since the paraxial regime is valid. As a consequence, dichroism signals for the Bessel beam and LG beam are identical (see Fig. 5). For a small target, the dichroism signals are sensitive to the particular localization of the target. This dependence becomes less pronounced if the size of the target increases. The dichroism signals corresponding to a flip of $\Lambda_X \Lambda_L$ even vanish for macroscopically extended targets. It was already shown analytically in Ref. [24] that the photoionization probability (14) of macroscopically extended targets, evaluated for the case of an ionizing Bessel beam, does not depend on m. Already a target size of 100 nm can, therefore, be described as a macroscopic target. The vanishing dichroism signals for the case of an XUV LG beam are explained by the argument of the similarity of two beams raised before. These signals also change sign abruptly at the angle $\theta_p = \pi/2$ and vanish on the plane perpendicular to the beam ($\theta_p = \pi/2$). In contrast, however, the signals associated with a flip of Λ_L (the circular dichroism) does not show a significant dependence on the target size.

Let us finally discuss the linearly polarized LG beam. Dichroism in plane-wave two-color experiments was investigated in the work of Kazansky *et al.* [37]. There, an unpolarized atomic target was considered that is irradiated by an XUV and a NIR pulse. It was analytically shown that the circular IR dichroism with linearly polarized XUV pulse tends to zero if the IR pulse is long. Although we replace their plane-wave XUV pulse with a twisted LG beam, all possible dichroism signals vanish or are too small compared to the case of circularly polarization. In Ref. [37], it was also shown that the dichroism increases if the long IR pulse is replaced with a short pulse. We can, therefore, summarize that the dichroism signals do not depend on characteristic parameters of beams if the NIR field is long and the XUV field is linearly polarized.

IV. CONCLUSIONS

In this paper, we investigated two-color ATI processes when a weak XUV vortex beam is assisted with a strong NIR field. As a vortex beam, we considered LG as well as Bessel beams. In the continuum, the photoelectron can absorb or emit one or several photons from the NIR laser field. Thus, sidebands appear next to the main XUV line in the photoelectron spectrum. Our investigations showed that the magnitude of these sidebands is affected by the location of the atomic target and the quantum numbers characterizing the vortex beam. Furthermore, we found that the circularly polarized LG and Bessel beams behave similarly in the paraxial approximation. In other words, calculated dichroism signals for these two cases are identical. The dichroism vanishes if the (infinitely long) LG pulse is linearly polarized. Our investigations open up ways for two-color experiments with twisted light beams in the paraxial and nonparaxial regimes. An interesting future work concern the extension of our paper to short XUV and NIR pulses where it has been shown for the plane wave that a nonvanishing linear-circular dichroism exists [37].

ACKNOWLEDGMENTS

The work reported in this paper was partially supported by the DFG Priority Programme 1840, "Quantum Dynamics In Tailored Intense Fields" under Contract No. FR 1251/17-1. B. Böning and W. Paufler acknowledge support from the Helmholtz Institute Jena and the Research School of Advanced Photon Science of Germany.

[1] P. Agostini, F. Fabre, G. Mainfray, G. Petite, and N. K. Rahman, Phys. Rev. Lett. **42**, 1127 (1979).
[2] G. G. Paulus, F. Lindner, H. Walther, A. Baltuška, E. Goulielmakis, M. Lezius, and F. Krausz, Phys. Rev. Lett. **91**, 253004 (2003).
[3] D. B. Milošević, G. G. Paulus, D. Bauer, and W. Becker, J. Phys. B: At. Mol. Opt. Phys. **39**, R203 (2006).
[4] T. E. Glover, R. W. Schoenlein, A. H. Chin, and C. V. Shank, Phys. Rev. Lett. **76**, 2468 (1996).
[5] P. O'Keeffe, R. López-Martens, J. Mauritsson, A. Johansson, A. L'Huillier, V. Véniard, R. Taïeb, A. Maquet, and M. Meyer, Phys. Rev. A **69**, 051401 (2004).
[6] M. Meyer, D. Cubaynes, D. Glijer, J. Dardis, P. Hayden, P. Hough, V. Richardson, E. T. Kennedy, J. T. Costello, P. Radcliffe, S. Düsterer, A. Azima, W. B. Li, H. Redlin, J. Feldhaus, R. Taïeb, A. Maquet, A. N. Grum-Grzhimailo, E. V. Gryzlova, and S. I. Strakhova, Phys. Rev. Lett. **101**, 193002 (2008).
[7] M. Meyer, D. Cubaynes, P. O'Keeffe, H. Luna, P. Yeates, E. T. Kennedy, J. T. Costello, P. Orr, R. Taïeb, A. Maquet, S. Düsterer, P. Radcliffe, H. Redlin, A. Azima, E. Plönjes, and J. Feldhaus, Phys. Rev. A **74**, 011401(R) (2006).
[8] M. Meyer, J. T. Costello, S. Düsterer, W. B. Li, and P. Radcliffe, J. Phys. B: At. Mol. Opt. Phys. **43**, 194006 (2010).
[9] J. Ortega, in *Free Electron Lasers 2002*, edited by K.-J. Kim, S. Milton, and E. Gluskin (Elsevier, Amsterdam, 2003), pp. 8–14.
[10] F. Ehlotzky, Phys. Rep. **345**, 175 (2001).
[11] P. Radcliffe, M. Arbeiter, W. B. Li, S. Düsterer, H. Redlin, P. Hayden, P. Hough, V. Richardson, J. T. Costello, T. Fennel, and M. Meyer, New J. Phys. **14**, 043008 (2012).
[12] H. Klar and H. Kleinpoppen, J. Phys. B: At. Mol. Phys. **15**, 933 (1982).
[13] A. M. Akulshin, R. J. McLean, E. E. Mikhailov, and I. Novikova, Opt. Lett. **40**, 1109 (2015).
[14] R. A. Müller, D. Seipt, R. Beerwerth, M. Ornigotti, A. Szameit, S. Fritzsche, and A. Surzhykov, Phys. Rev. A **94**, 041402 (2016).
[15] M. Beijersbergen, R. Coerwinkel, M. Kristensen, and J. Woerdman, Opt. Commun. **112**, 321 (1994).
[16] J. Arlt and K. Dholakia, Opt. Commun. **177**, 297 (2000).
[17] N. R. Heckenberg, R. McDuff, C. P. Smith, and A. G. White, Opt. Lett. **17**, 221 (1992).
[18] C. Hernández-García, A. Picón, J. San Román, and L. Plaja, Phys. Rev. Lett. **111**, 083602 (2013).
[19] P. R. Ribič, D. Gauthier, and G. De Ninno, Phys. Rev. Lett. **112**, 203602 (2014).
[20] C. T. Schmiegelow, J. Schulz, H. Kaufmann, T. Ruster, U. G. Poschinger, and F. Schmidt-Kaler, Nat. Commun. **7**, 12998 (2016).
[21] G. F. Quinteiro, D. E. Reiter, and T. Kuhn, Phys. Rev. A **95**, 012106 (2017).

[22] B. Böning, W. Paufler, and S. Fritzsche, Phys. Rev. A **96**, 043423 (2017).
[23] B. Böning, W. Paufler, and S. Fritzsche, Phys. Rev. A **98**, 023407 (2018).
[24] D. Seipt, R. A. Müller, A. Surzhykov, and S. Fritzsche, Phys. Rev. A **94**, 053420 (2016).
[25] T. Mazza, M. Ilchen, A. J. Rafipoor, C. Callegari, P. Finetti, O. Plekan, K. C. Prince, R. Richter, M. B. Danailov, A. Demidovich, G. De Ninno, C. Grazioli, R. Ivanov, N. Mahne, L. Raimondi, C. Svetina, L. Avaldi, P. Bolognesi, M. Coreno, P. O'Keeffe, M. Di Fraia, M. Devetta, Y. Ovcharenko, Th Möller, V. Lyamayev, F. Stienkemeier, S. Düsterer, K. Ueda, J. T. Costello, A. K. Kazansky, N. M. Kabachnik, and M. Meyer, Nat. Commun. **5**, 3648 (2014).
[26] D. M. Wolkow, Z. Phys. **94**, 250 (1935).
[27] D. Bauer, D. B. Milošević, and W. Becker, Phys. Rev. A **72**, 023415 (2005).
[28] L. W. Davis, Phys. Rev. A **19**, 1177 (1979).
[29] O. Matula, A. G. Hayrapetyan, V. G. Serbo, A. Surzhykov, and S. Fritzsche, J. Phys. B: At. Mol. Opt. Phys. **46**, 205002 (2013).
[30] D. L. Andrews and M. Babiker, *The Angular Momentum of Light* (Cambridge University Press, New York, 2012).
[31] A. A. Peshkov, D. Seipt, A. Surzhykov, and S. Fritzsche, Phys. Rev. A **96**, 023407 (2017).
[32] L. Allen, M. W. Beijersbergen, R. J. C. Spreeuw, and J. P. Woerdman, Phys. Rev. A **45**, 8185 (1992).
[33] G. Vallone, Opt. Lett. **42**, 1097 (2017).
[34] H. A. Haus, *Waves and Fields in Optoelectronics* (Prentice-Hall, Englewood Cliffs, NJ, 1984).
[35] P. Lambropoulos, Phys. Rev. Lett. **29**, 453 (1972).
[36] G. Watson, *A Treatise on the Theory of Bessel Functions* (Cambridge University Press, New York, 1944).
[37] A. K. Kazansky, A. V. Grigorieva, and N. M. Kabachnik, Phys. Rev. A **85**, 053409 (2012).